



# Flexible and highly sensitive graphene/carboxymethyl cellulose films for bending sensing

Ping Liu<sup>1</sup> · Minggan Chen<sup>1</sup> · Canguang Xiong<sup>1</sup> · Xiuhua Cao<sup>2</sup> · Hui Wang<sup>1</sup>

Received: 24 December 2019 / Accepted: 8 July 2020 / Published online: 20 July 2020  
© Springer Science+Business Media, LLC, part of Springer Nature 2020

## Abstract

High sensitivity is the major desired requirements of strain sensors for wearable electronics applications, especially in health and medical monitoring. A bending sensor attach tightly to skin remains a hot topic considering wide response range and high sensitivity. Herein, a highly sensitive strain sensor based on graphene/carboxymethyl cellulose (GE/CMC) composite film is fabricated through vacuum filtration and chemical reduction. CE/CMC films present an ordered multi-layer structure, which is helpful for signal sensitivity. Owing to the super flexibility of carboxymethyl and the excellent electrical and mechanical properties of GE, the free-standing GE/CMC film reveals high conductivity at  $1321.9 \text{ S m}^{-1}$ , good response performance at low voltage driving of 1 mV. The bending signal of GE/CMC film was stable, when applying 0–90° forward bending strain. Its sensitivity reaches at  $0.83 \text{ rad}^{-1}$ , and response time of 90° forward bending strain is less than 190 ms, with a regularly stable bending signal response in 100 cycles bending testing. With such outstanding performances, the GE/CMC film can be expected to be applied in motion signal detection.

## 1 Introduction

Strain sensors are becoming increasingly popular because of their wide potential applications in areas including human motion detection, health monitoring and human–machine interaction [1, 2]. In general, strain sensors can convert mechanical deformation signals to electrical signals owing

to the capacitive [3], piezoelectric and piezoresistive effect [4–6]. Wearable strain sensors for health monitoring [7], joint motion [8], robots [9] etc. possess many features such as good tensile properties, continuous monitoring, flexibility, stability, and portability. Traditional strain sensors use metallic materials or semiconductor materials as sensitive layers, which are difficult to meet the needs of highly flexibility and complex three-dimensional strain measurement. To date, conductive composites have aroused considerable concern out of excellent flexibility, low cost, and good processability. These composites are hopeful use as candidates for strain sensing materials [10, 11].

Two-dimensional materials, such as graphene [12], are considered effective polymer fillers and attractive for both conventional semiconductor applications and field in flexible electronics [13]. Graphene based strain sensors have achieved rapid development recently [14]. Assembled graphene films show relatively poor electrical conductivity and mechanical property owing to the poor interlayer junction contact resistance and the structural defects formed during the vigorous exfoliation and reduction processes [15]. Traditional graphene/polymer flexible strain sensors fail to simultaneously attain wide response range and high sensitivity because of the existence of organic materials with lower electrical performed shorter service life. For example, Jin et al. reported graphene film sensor with the highest linear

**Electronic supplementary material** The online version of this article (<https://doi.org/10.1007/s10854-020-03966-8>) contains supplementary material, which is available to authorized users.

✉ Hui Wang  
wanghui@scut.edu.cn

Ping Liu  
laliuping@163.com

Minggan Chen  
chenmg1996@163.com

Canguang Xiong  
82765432@163.com

Xiuhua Cao  
caoxh@china-fenghua.com

<sup>1</sup> College of Materials Science & Engineering, South China University of Technology, Guangzhou 510640, China

<sup>2</sup> State Key Laboratory of Advanced Materials and Electronic Components, Guangdong Fenghua Advanced Technology Holding Co., Ltd., Zhaoing 526020, China

fitting degree between resistance change rate and pressure, but it is effective within pressure range of 40 to 670 Pa [13]. In addition, the complicated manufacturing procedures of these strain sensors are not suitable for large-scale production [16]. Pang et al. demonstrated a mechanical sensor with graphene porous network (GPN), but it is tough for large-scale production employing the chemical solution to etch the nickel foam template coated with multilayer graphene [17]. Li et al. investigated graphene woven fabrics (GWFs) for strain sensing by atmospheric pressure CVD method, etching, transferring, and rinsing. The electrical resistance of GWFs increases exponentially with tensile strain with gauge factors of  $10^3$  under 2–6% strains and  $\sim 10^6$  under higher strains [14].

Carboxymethyl cellulose (CMC) is produced by partial substitution of the 2, 3, and 6 hydroxyl groups of cellulose by carboxymethyl groups. It is a valuable material for ecological friendliness, low cost, high utilization efficiency, biodegradability, and renewability. Biodegradable CMC has many hydrophilic groups on the molecular chain, as well as a large molecular surface area [18]. Besides, CMC is hydrophilic and adhesive, so graphene oxide disperses evenly in its solution. The cross-linking of CMC chains contributes to its multi-dimensional network. Therefore, CMC aqueous solution exhibits high viscosity at low concentrations [19]. In our previous work, the prepared graphene/carboxymethylcellulose (GE/CMC) aerogel exhibits a porous structure, which shows stable high elasticity (4000 steady compression cycles at 50% strain) and superior electrical conductivity ( $86.73 \text{ S m}^{-1}$  under 70% compression strain) [20].

In this work, conductive graphene oxide/carboxymethyl cellulose (GO/CMC) composite films were fabricated via a facile and scalable vacuum filtration method. Graphene/carboxymethyl cellulose (GE/CMC) free-standing films were obtained by chemical reduction. Finally, the obtained GE/CMC free-standing films were embedded in silicone rubber to reduce measurement errors caused by touching. The conductive films, applied bending strain and bending rate on the sensing behaviors were investigated by both bending and cyclic bending-releasing tests. Moreover, a schematic illustration of piezoresistive effect of these GE/CMC free-standing films under bending was drawn for a better understanding of the strain sensing mechanism.

## 2 Experimental methods

### 2.1 Materials and reagents

Graphite flakes (325 mesh) and carboxymethyl cellulose (CMC, M.W. 250,000, DS = 0.9) were purchased from Shanghai Aladdin Biochemical Technology Co., Ltd. Hydrogen peroxide ( $\text{H}_2\text{O}_2$ , 30 wt%), and ethanol (EtOH, 99.7 wt%)

were supplied by Tianjin Fuyu Fine Chemical Co., Ltd. Potassium permanganate ( $\text{KMnO}_4$ , 99.5 wt%), Sodium nitrate ( $\text{NaNO}_3$ , 99 wt%), concentrated sulfuric acid ( $\text{H}_2\text{SO}_4$ , 98 wt%), hydrochloric acid (HCl, 36–38 wt%), and phosphorus pentoxide ( $\text{P}_2\text{O}_5$ , 98 wt%) were provided by Guangzhou Chemical Reagent Factory. Hydroiodide was provided by Shanghai Maclean Biochemical Technology Co., Ltd. Silicone Rubber (Dow Corning 184) was purchased from Dow Corning Silicone Co., Ltd. Deionized water was made from LEDING ultra-pure water machine. All reagents were used as received without further purification.

### 2.2 Preparation of GO and free-standing GE/CMC film fabrication

Graphite oxide (GO) was prepared according to improved Hummer's method [21]. Graphite (4 g) and  $\text{NaNO}_3$  (2 g) was cast into a 1000 ml three-necked flask. Then, 90 ml of concentrated  $\text{H}_2\text{SO}_4$  (pre-frozen) was poured into flask and stirring started with ice-bath outside. Finely grounded  $\text{KMnO}_4$  was added to flask slowly to control the temperature of the reaction system under  $5^\circ\text{C}$ . The low-temperature stage sustained for 4 h. Then the ice bath was removed and the suspension was heated to  $35^\circ\text{C}$  for 2 h. Then, 140 ml of deionized water was added dropwise, and the temperature was maintained at about  $95^\circ\text{C}$  for 15 min. The suspension was poured into 600 ml of deionized water ( $60^\circ\text{C}$ ) while stirring, and treated with appropriate amount of  $\text{H}_2\text{O}_2$  solution (30%), and washed with diluted HCl solution and water until the pH value closes to 7. Finally, the GO was obtained after freeze-drying.

The required amount of GO was dispersed in water and sonicated for 2 h at an output power of 100 W using a digital ultrasonic processor (SK2200H, Shanghai KeDao) in water bath at room temperature. Then, 0 mg, 27 mg, 60 mg, 103 mg of CMC (CMC to 0 wt%, 10 wt%, 20 wt%, 30 wt% of total solute content, respectively) was added to the solution, respectively. The solution was stirred at  $40^\circ\text{C}$  for 4 h, and kept still for another 24 h. The GO/CMC films were obtained by filtration with a microporous PTFE membrane (pore size of  $0.45 \mu\text{m}$ ). Those films were dried for 6 h and each film was pressed under 2 kg weight for 1 min. The free-standing GE/CMC films were obtained by reduction in hydrogen iodide acid solution at  $70^\circ\text{C}$  for 1 h. Then, they were washed with ethanol and immersed in it for 24 h, and dried for 6 h under vacuum at room temperature.

The above GE/CMC films were embedded in silicone rubber for 2 h, then cured in an oven at  $55^\circ\text{C}$  for 2 h. The composite films with a flexible silicone rubber substrate were finally obtained. Here, we named the GO/CMC films with CMC content of 0 wt%, 10 wt%, 20 wt%, 30 wt% as GO/CMC-0, GO/CMC-10, GO/CMC-20, GO/CMC-30. Those films reduced

with hydriodide were sequentially named GE/CMC-0, GE/CMC-10, GE/CMC-20, GE/CMC-30, respectively.

### 2.3 Characterization

The cross-sectional (gashed by a sharp blade) morphology of composite film were characterized using a field emission scanning electron microscope (SEM, ZEISS EVO18, Carl Zeiss Co., Ltd., Oberkochen, Germany). All the samples were sputter coated with platinum. Wide-angle X-ray diffraction (XRD) patterns were taken with 40 kV, 450 mA Cu Ka (the X-ray wave length is 1.54178 Å) radiation using a Panalytical X'pert PRO (PANalytical B.V., Netherlands). Fourier transform infrared (FTIR) spectra of aerogels were obtained with VERTEX 70 spectrometer (Bruker Company, Germany). The Raman spectra of the samples were collected via a LabRAM Aramis Raman spectroscopy (HORIBA Jobin Yvon, France). X-ray photoelectron spectroscopy (XPS) was carried out using a 250Xi electron spectrometer (Thermo Fisher Scientific Co., Ltd., America). Zeta potential was measured by Zetasizer NANO ZS9 (Malvern company, the United Kingdom).

Young's moduli were measured by Instrument DMA Q800. Samples were cut into 30 mm × 6 mm size for testing the stress–strain curves.

Electrical conductivity was measured by four-probe meter (RTS-9, Guanandgzhou Four-probe Technology Co., Ltd., China). The electrical conductivity of the film was calculated using  $R = 1/(\sigma \times A)$ , where  $\sigma$  (S/cm) is the electrical conductivity,  $R$  (X) is the electrical resistance, and  $A$  (cm<sup>2</sup>) is the cross-section area of the film.

The bending strain sensing performance was measured with CS2350 electrochemical workstation (Koster Instrument Co., Ltd.).

The bending sensitivity of films was calculated by formula (1):

$$BS = \frac{\frac{\Delta R}{R_0}}{\theta} = \frac{\frac{|R_0 - R|}{R_0}}{\theta} \quad (1)$$

$R_0$  is the resistance of unbending film,  $R$  is the real-time resistance of film when bending, and  $\theta$  is the corresponding

bending angle. The bending angle is controlled by a self-made bending device. The positive and negative electrodes are connected to the two ends of GE/CMC films. Forward bending and backward bending are applied to GE/CMC films, and the current changes of films are recorded by the electrochemical workstation. Then, current changes are converted to resistance changes by Ohm's law.

## 3 Results and discussion

### 3.1 Formation and composition analysis of films

Figure 1 shows the synthesis procedure of free-standing GE/CMC films. The GE/CMC films with different CMC loadings exhibit a metallic luster under sun light, as shown in Fig. 2. However, the edge part of GE/CMC-0 and GE/CMC-10 is easy to collapse after the reduction of hydriodic acid. The samples of GE/CMC-20 and GE/CMC-30 are relatively uniform, and they have good flexibility as can be seen from Fig. 2g and h. The proper content of CMC is helpful for effective assembling between graphene sheets.

To study the composition of films and the possible interaction between GE and CMC, we discussed the results of FT-IR and XPS. Figure 3 shows the infrared spectra of four graphene films of composite 0–30 wt% CMC. The wave number of 2973 cm<sup>-1</sup> corresponds to the stretching vibration peak of the common hydrocarbon group (–CH) in GE/CMC-0. The variation of the dipole moment of the common hydrocarbon group is weak in the infrared test. With the increase of CMC content, the internal chemical environment of the composite film becomes more complicated. The hydrocarbon-based stretching vibration peaks near the wave number of 2973 cm<sup>-1</sup> in GE/CMC-10, GE/CMC-20, and GE/CMC-30 become weaker. The wave number of 2910 cm<sup>-1</sup> corresponds to methyl group (–CH<sub>3</sub>) stretching vibration peaks. The stretching and vibration coupling of the hydrocarbon base peak has a small polarity, the corresponding methyl peak is weak consequently. 1615 cm<sup>-1</sup> and 1725 cm<sup>-1</sup> correspond to the stretching vibration of the graphene skeleton C=C and the oxygen-containing

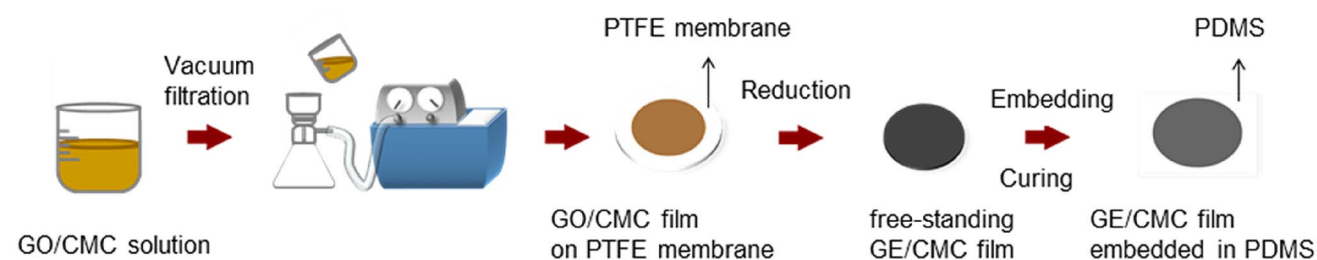
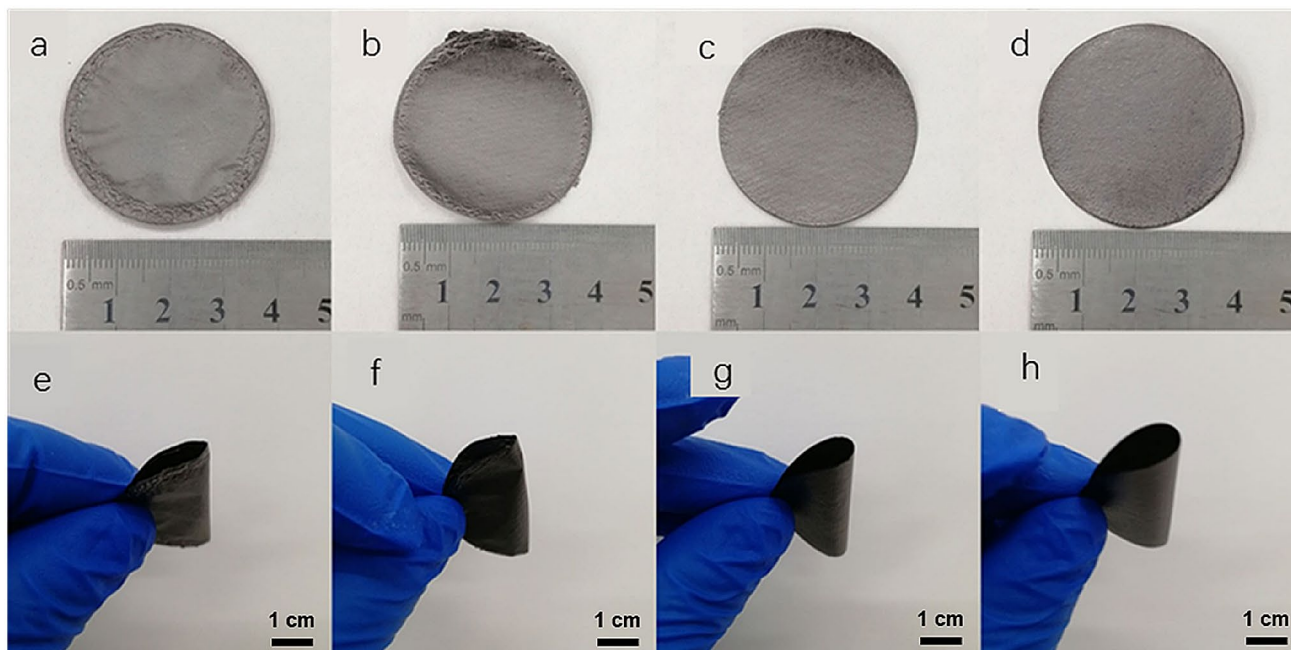
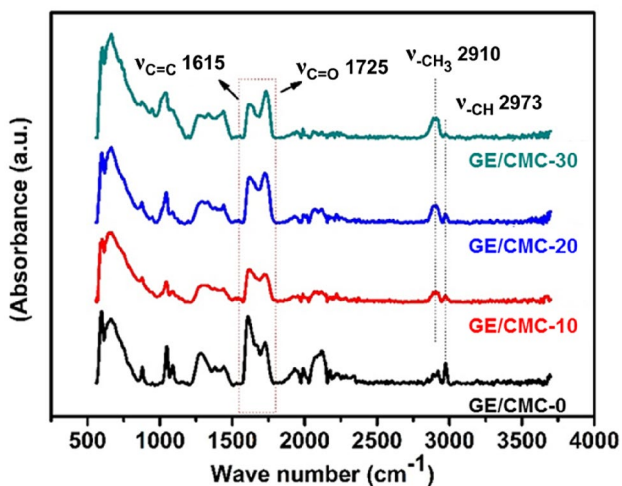


Fig. 1 Schematic diagram of preparing GE/CMC film



**Fig. 2** Apparent appearance of graphene films: **a** and **e** GE/CMC-0, **b** and **f** GE/CMC-10, **c** and **g** GE/CMC-20, **d** and **h** GE/CMC-30



**Fig. 3** FTIR spectra of GE/CMC-0, GE/CMC-10, GE/CMC-20, GE/CMC-30

functional group C=O bond respectively, and the oxygen content still exists after the graphene film (GE/CMC-0) was reduced. There are ester groups ( $-\text{COOR}$ ) in CMC chains. With the increase of CMC concentration, the concentration of ester carbonyl group increases, resulting in the increase of absorption peak intensity of carbonyl group (C=O). With the increase of CMC concentration, the structure of graphene is affected. The characteristic peak intensity of C=C bond decreases gradually because: when CMC is added, the structure of substituent groups on both sides of C=C bonds

becomes more symmetrical, resulting in the decrease of dipole moment and peak intensity.

Figure 4 shows the XPS spectra of GE/CMC-0, GE/CMC-10, GE/CMC-20, and GE/CMC-30 (The C1s spectra (XPS) and wide-scan spectrums). In the high-resolution spectrum of C1s, the 284.8 eV electron binding energy corresponds to the peak of C-C/C=C. For C-O and C=O, the electron binding energy of C-O increased from 285.6 to 286.3 eV with the increase of CMC content. Similarly, the electron binding energy of C=O increased from 288 to 288.9 eV. The electron binding energy of the carbon-oxygen bond shifting toward higher binding energy. It may be explained by the change in the chemical environment around the atoms in the molecule with the increase in CMC. The addition of CMC expands the layer spacing and weakens the effect of  $\pi-\pi$  stacking in graphene sheets. The high electron binding energy represents a more stable chemical state. The hydrogen bond (around the internal oxygen-containing functional groups) interactions lead to peak displacement. In addition, wide-scan spectrums of four different CMC film, the film mainly contains four elements, namely C, O, N and I. The N element was mainly introduced in the oxidation process of graphite. The I element was introduced by hydroiodic acid. The N element is not more than 8 wt%, and the I element is not more than 2 wt%. As the CMC content increases, the carbon/oxygen mass ratio ( $\text{AR}_{\text{C/O}}$ ) of the GE/CMC film decreases from 9.07 to 3.5, and the addition of CMC introduces a large amount of carboxyl groups, which increases the oxygen content in the film.



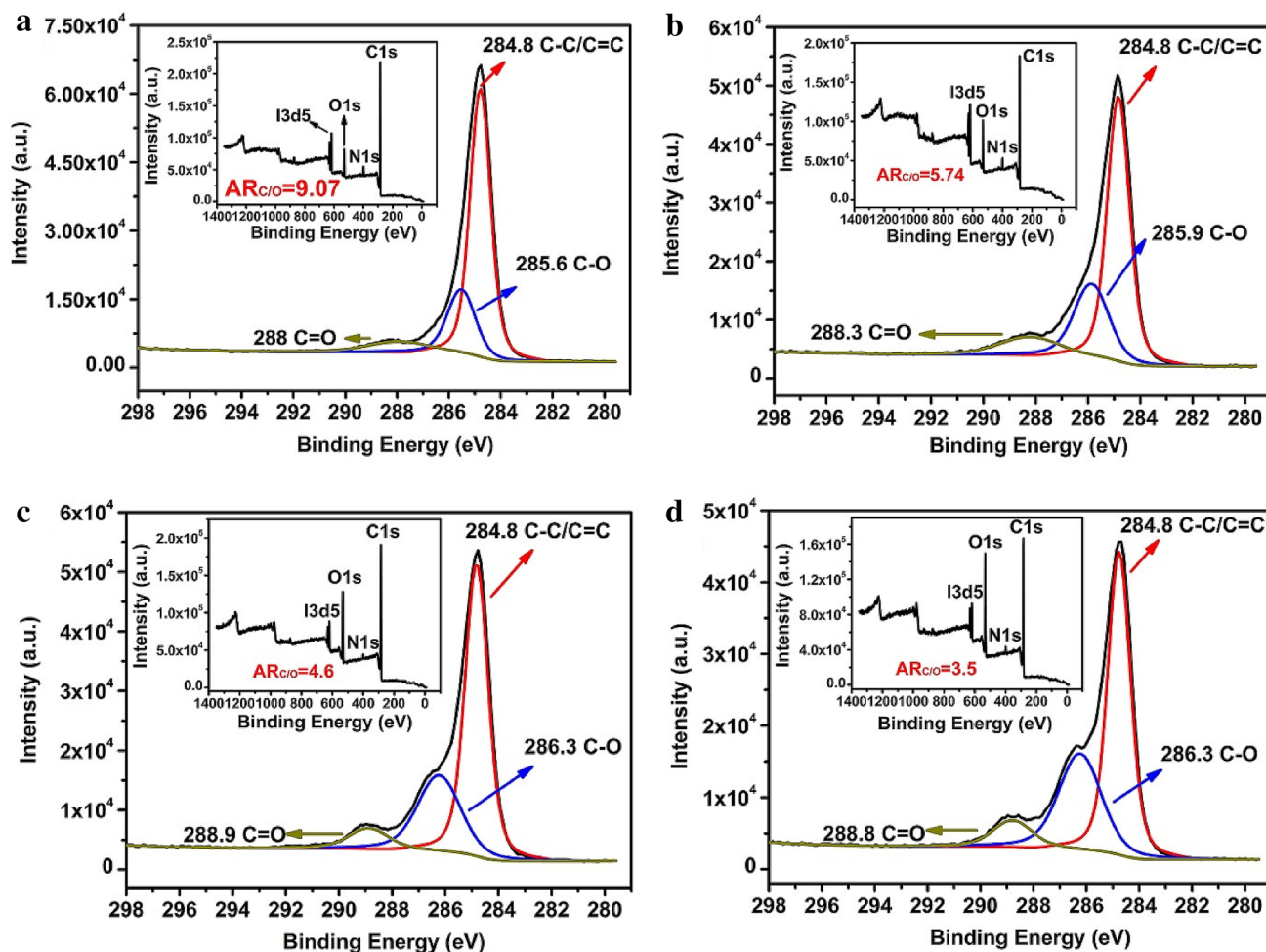


**Fig. 4** a–d The C1s spectra (XPS) of GE/CMC-0, GE/CMC-10, GE/CMC-20, GE/CMC-30. *Inset* wide-scan spectrums exhibit the composition of the elements of films

### 3.2 Morphology and structure

To investigate influence of GE/CMC dispersions on the morphological properties, SEM images of free-standing films with different CMC loadings are shown in Fig. 5. The cross-section morphology of GE/CMC films exhibited a layer-by-layer structure. The films are mainly composed of graphene sheets. After reduction, the graphene sheets are closely packed together by  $\pi$ - $\pi$  bonds. The graphene sheets are stacked very tightly without CMC in Fig. 5a. As the CMC content increases, a large number of gaps occur between the film sheets, because the interaction between CMC chains and graphene sheets hinders their close packing. The large gaps enable the film responses quickly to deformation, which are helpful for sensing property.

### 3.3 Electrical properties

The GE/CMC films with different CMC content were reduced in hydriodic acid at 70 °C for 1 h, and then rinsed with ethanol for several times. The conductivity of films is shown in Table 1. As the CMC content increases, the conductivity of the films tends to decrease. The formation of delocalized  $\pi$  bond between graphene sheets, along with the presence of movable electrons, contributes to the conductivity of the graphene films. When CMC was involved, CMC chains between the graphene sheets hinders the formation of delocalized  $\pi$  bond, thus decreases the directional electrons movement between graphene sheets. Materials with high conductivity do not necessarily meet the needs for sensor. For example, when the metal composite material with good conductivity is deformed,

**Fig. 5** Cross-section SEM images of GE/CMC films: **a** GE/CMC-0, **b** GE/CMC-10, **c** GE/CMC-20, **d** GE/CMC-30

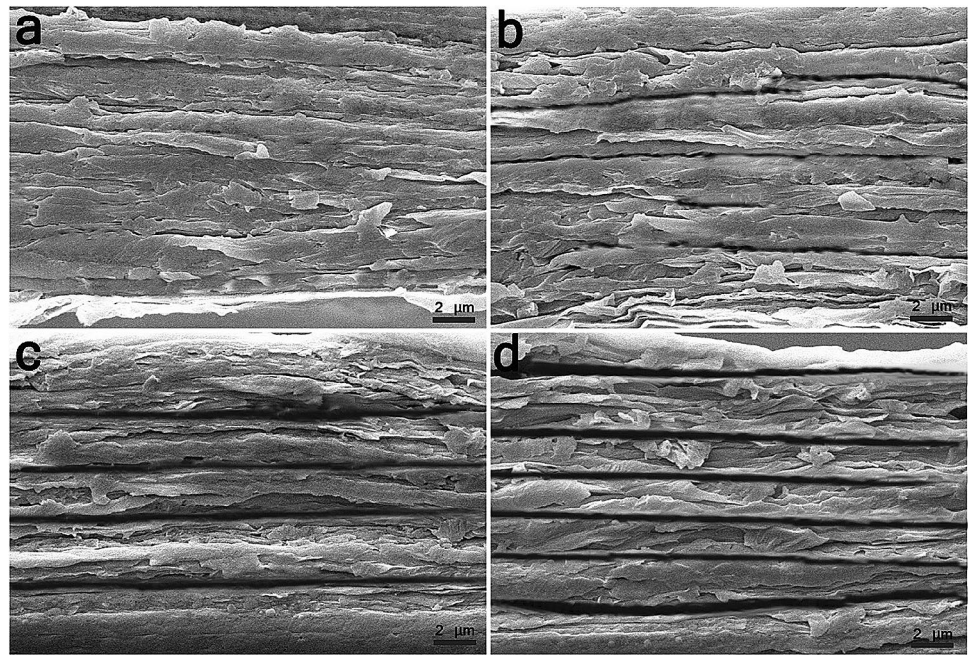


**Table 1** Conductivity of GE/CMC film

Sample	Conductivity ( $S m^{-1}$ )
GE/CMC-0	7930.2
GE/CMC-10	4338.6
GE/CMC-20	3657.4
GE/CMC-30	1321.9

the resistance change is small, and its sensing performance is limited.

### 3.4 Bending recovery behavior and sensing performance

We studied the sensing performance of GE/CMC-0, GE/CMC-10, GE/CMC-20 and GE/CMC-30 composite films in two bending conditions at  $90^\circ$  when applying 1 mV constant voltage, the two bending conditions were shown in Fig. 6. As shown in Fig. 7, the currents of GE/CMC-0, GE/CMC-10, GE/CMC-20 and GE/CMC-30 films are 0.87 mA, 0.3 mA, 0.093 mA and 0.032 mA at a constant voltage of 1 mV without bending. With the increase of

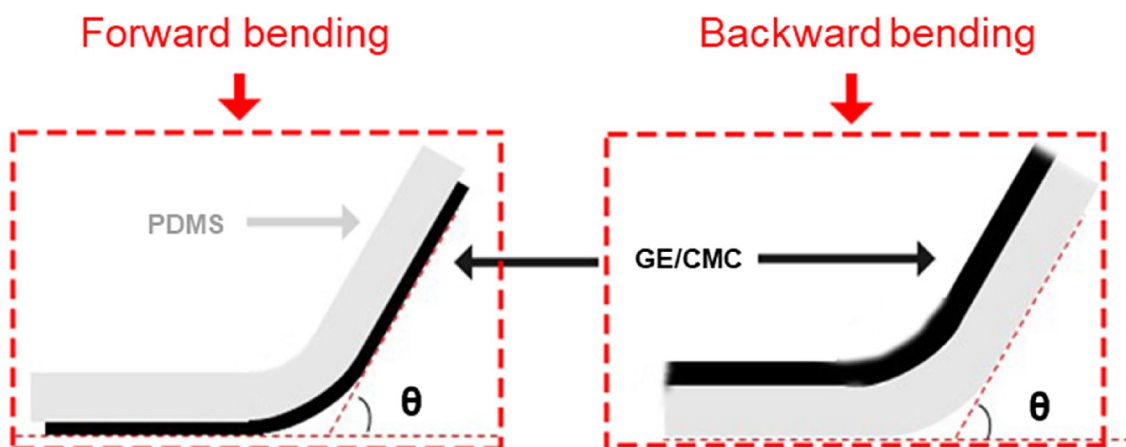


**Fig. 6** Two bending conditions

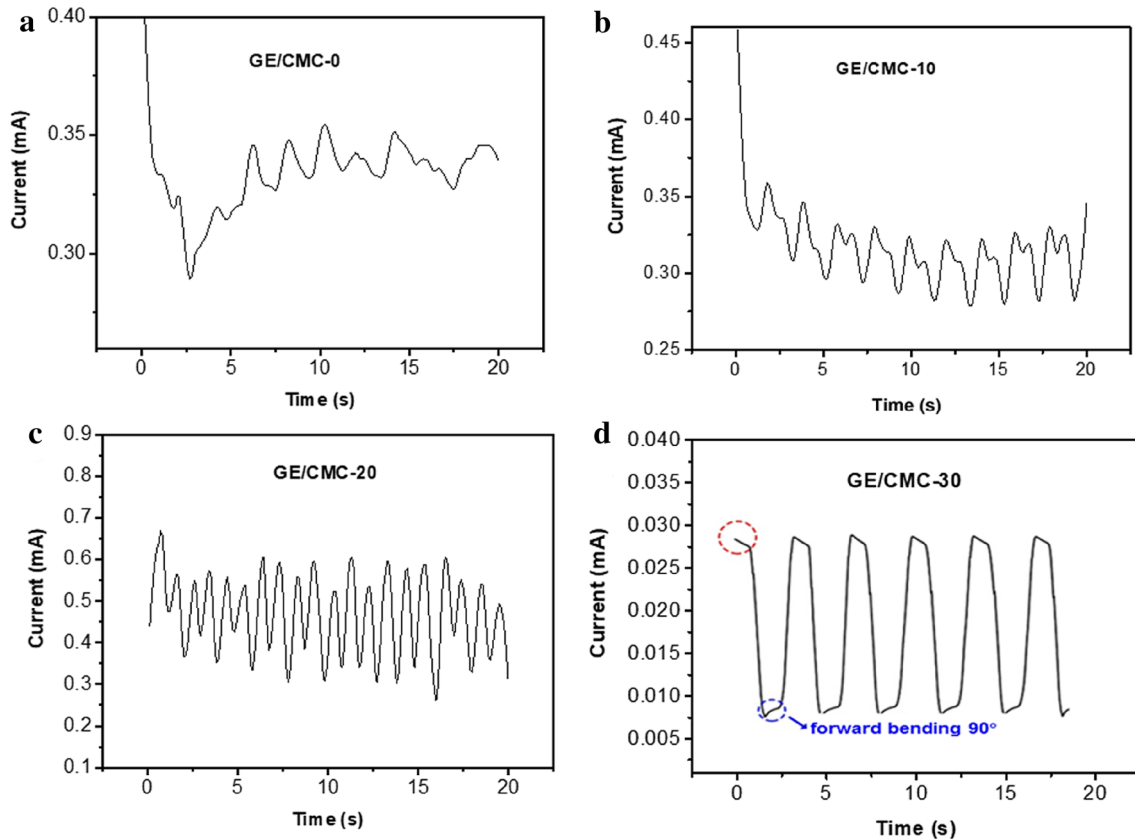


**Fig. 7** Currents of GE/CMC-0, GE/CMC-10, GE/CMC-20 and GE/CMC-30 Composite films with 1 mV constant voltage during 90° forward bending

CMC content, the current of the composite film decreases at the same voltage, indicating that the resistance of the film increases sequentially. This trend is consistent with Table 1. Figure 7 indicates GE/CMC-0, GE/CMC-10 and GE/CMC-20 samples having irregular signals when the films bent. More gaps are beneficial to regular responses when applying bending strain. In addition, when bending

angle increases, the electric current decreases and the film's resistance increases simultaneously). The bending angle exists and increases, and the tension in bending area increases, resulting in decrease in contact area of the graphene sheets and increases the electrical resistance. When the GE/CMC-0, GE/CMC-10, and GE/CMC-20 films are bent backwards, the current signals are irregular either.

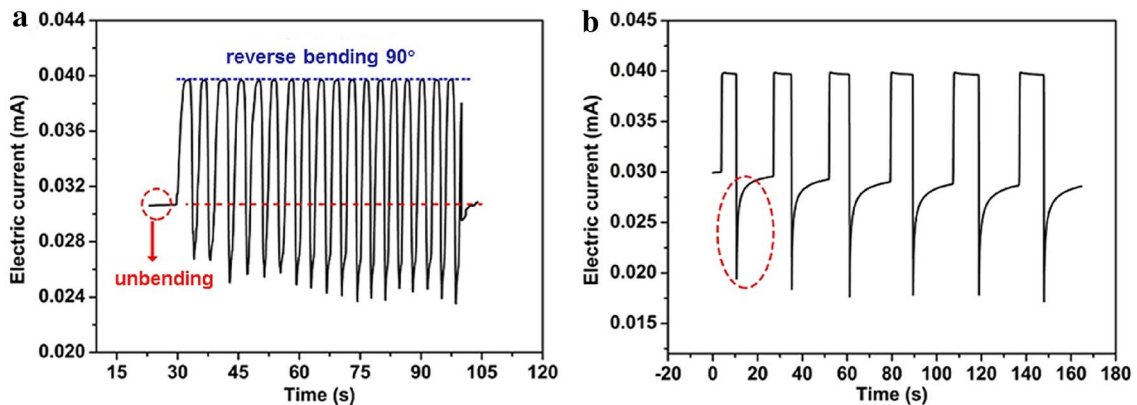


**Fig. 8** GE/CMC-30 films, **a** 90° backward fast bending cycles. **b** 90° backward slow bending cycles



The electrical responses are also consistent with morphology results.

When applying backward bending cycles 0 to 90°, the GE/CMC-30 film bending back in about 4 s was set for one cycle. As shown in Fig. 8, the initial current is 0.031 mA. During backward bending cycles for 20 times, the current signals maintained stable at 0.04 mA, indicating that the real time resistance of film is decreased with the increasing bending angle. The graphene layers was backwards bent, a large compressive stress exists near the bending area, which enable the graphene sheets contact more tight and the resistance decreases. When the film returned to 0° bending, the current appears unstable. A decrease in the instantaneous current is related with an increase in the instantaneous resistance. Figure 8b shows that when 90° backward bending cycle was applied slowly, the current will decrease instantaneously and then slowly return to 0.03 mA. This phenomenon is caused by a hysteresis effect from an unstable state to a stable state. When graphene sheets change state suddenly, the instantaneous tension between the graphene sheets makes the contact of the graphene sheets unstable, resulting in an instantaneous decrease in current.

We further investigated the stability of GE/CMC-30 film under long-term 90° forward bending cycles conditions. As shown in Fig. 9, we performed a bending electrical signal response cycle test on the GE/CMC-30 film for about 100 times. It can be seen that the curve cycles stable, and the current value stables at 0.01 mA when bending angle reaches to 90°. Two partial curves during 0 to 50 s and 210 to 260 s clearly exhibit a wave form. The signal curve is relatively regular, which indicates the GE/CMC-30 film possess certain fatigue resistance, making it possible for the bending sensor application. Similar to the backward bending, the GE/CMC-30 film also has a sudden change in current when the forward bending angle returns to 0°. And the critical abrupt current is higher than the steady state current.

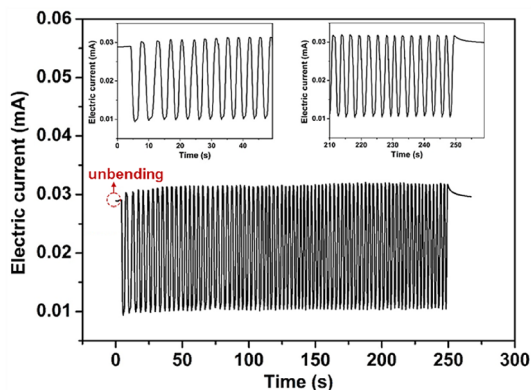


Fig. 9 Cycling stability test of GE/CMC-30 film from 0° to 90° forward bending

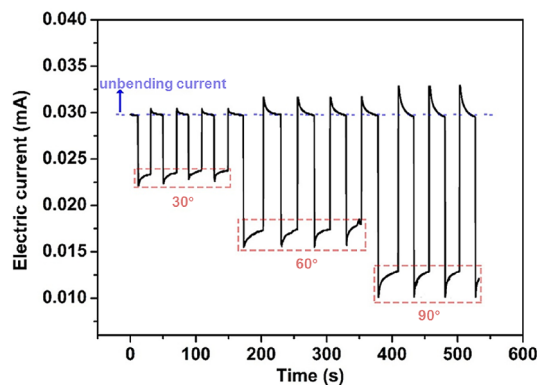


Fig. 10 Mutation and hysteresis effect of current in GE/CMC-30 films with different forward bending angles

Figure 10 shows the current curve of the GE/CMC-30 film when forward bending of 30°, 60° and 90°. The initial current is 0.03 mA, and the current curve corresponds to different forward bending angles exhibit good regularity. However, a sudden change in current (higher than the initial 0.03 mA) occurs before it returns to a steady state when the bending returns to the initial state. The reason for the sudden change of the forward bending current is similar to that of the backward bending discussed above. When the forward bending is performed, the contact area between the graphene sheets is decreased due to the larger tension. When quick returning to the initial unbent state, the originally tensioned graphene sheets are squeezed instantaneously, resulting in an increase in current. After being stabilized, the conductive structure is restored and then the current reaches a stable state at 0.03 mA. It is worth noting that as the bending angle increases, the larger tension is restored and a larger change in the abrupt current. Similarly, when the critical angles of forward bending are 30°, 60° and 90°, there are hysteresis effects of current. When bending to these critical angles, the

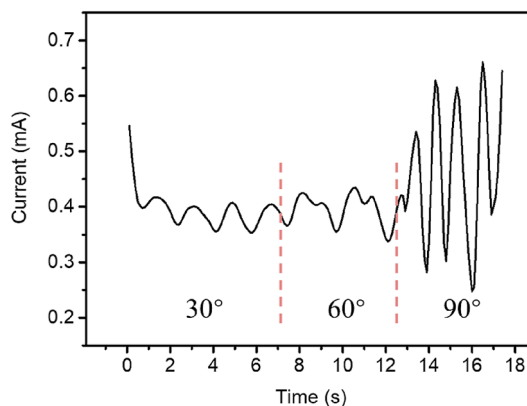
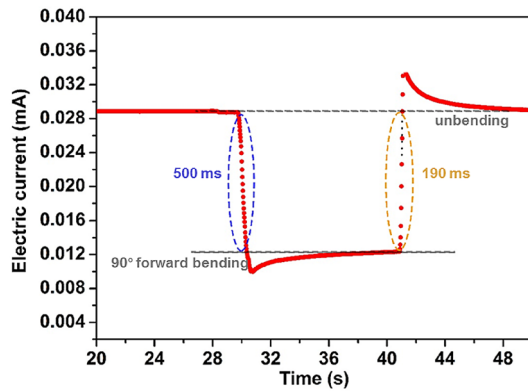
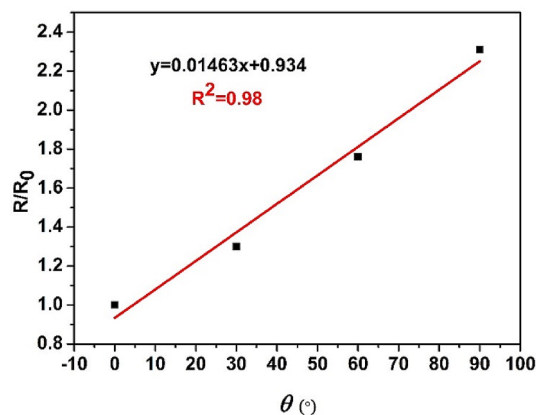


Fig. 11 Electrical current of GE/CMC-30 film with different backward fast bending angles





**Fig. 12** Response time of GE/CMC-30 from 0 to 90° forward bending



**Fig. 13** The fitting curve of the relative resistance  $R/R_0$  of GE/CMC-30 and the forward bending angle

instantaneous large bending angle changes the original layer structure, resistance increases and current decreases. The graphene sheet current reaches a steady state corresponding to 0.023 mA, 0.017 mA, and 0.013 mA, respectively.

Figure 11 shows that GE/CMC-30 does not have a linear relationship between current and bending angles when

the film is backward bent. The electrical current stabilizes at 0.355 mA in 30° backward bending angle, 0.343 mA in 60°, and 0.302 mA in 90°.

The response time reflects the speed of the film during loading and unloading cycle. Figure 12 shows the response time of GE/CMC-30 film from 0° to 90° after the signal was stable. Considering that the signal after the final stabilization is consistent with the initial value, the response time was measured from 0° to 90°. The response time during one fast bending cycle from 0° to 90° is 500 ms, and from 90° to 0° is about 190 ms. Considering that the bending speed is affected by the operator's bending speed, the actual response time should be less than 190 ms.

Figure 13 shows the GE/CMC-30 film forward bending scatter plot and linear fit of the relationship between relative resistance  $R/R_0$  and the bending angle  $\theta$  (0°, 30°, 60° and 90°). The real-time resistor  $R$  equals to ratio of voltage to current, and  $R_0$  is the initial resistance without bending. The linear relationship of the relative resistance  $R/R_0$  to the bending angle  $\theta$  reaches 0.98. The forward bending strain sensitivity value (BS) of the GE/CMC-30 film calculated by the formula (1) reaches to  $0.83 \text{ rad}^{-1}$ , which is higher than the sensitivity of most bending sensing materials (Table 2) [4, 9, 22–24]. This GE/CMC film has obvious signal feedback during bending cycles, making it hopeful for bending sensor application.

It is a common choice to utilize the piezoresistive effect of materials to make a stress sensor. The piezoresistive effect of graphene sensor can be summarized as three points. (1) The intrinsic piezoresistive properties of graphene [25]. When strain is applied to graphene materials, the energy band gap of single graphene changes. (2) The change of contact area of graphene sheets. It leads to the resistance change of the whole material. (3) The tunneling effect between adjacent graphene layers [26]. The main sensing mechanisms of GE/CMC is the change of contact area. According to Fig. 5, the GE/CMC-0 does not form a layer-by-layer structure. When bending stress is applied, the GE/CMC-0 shows irregular signals. With the increase of CMC content, the

**Table 2** Properties of the different bending strain-sensing materials

Bending samples	Response time (ms)	Conductivity	Bending sensitivity ( $\text{rad}^{-1}$ )	REFERENCES
rGO/SA-3	–	–	0.172	[22]
PGA	< 78	$45 \text{ S m}^{-1}$	0.26	[23]
AgNWs/LDH	< 105	$10^4 \text{ S m}^{-1}$	0.16	[24]
PDCY–RGO	< 100	–	0.19	[4]
AuNWs/PANI	–	–	0.83	[9]
GE/PDMS	33	–	$2.36 \times 10^4$	[27]
GE/ polymer	20	–	12.8	[28]
GE sensor	< 4	$\sim 100 \text{ K}\Omega/\square$	> 500	[26]
GE/CMC-30	< 190	1321.9	0.83	This work

multilayer structure and interlayer gap of films become apparent. Sequentially, films have a good response signals to the change of bending stress. In materials containing both low resistance (GE) and high resistance (CMC), the sensing performance is mainly related to the change of contact area between graphene layers.

## 4 Conclusion

In this work, graphene/carboxymethyl cellulose (GE/CMC) composite films with different concentration ratios are obtained by facial vacuum filtration and chemical reduction. The obtained GE/CMC film is coated with a layer of 1 mm thick silicone rubber to improve the bending workability for bending sensing test. The conductivity of the obtained GE/CMC-30 film is  $1321.9 \text{ S m}^{-1}$  and has good response at low driving voltage of 1 mV. The sensing signal of GE/CMC-30 film is stable when applying forward bending strain from 0 to  $90^\circ$ . The response time of forward bending strain  $90^\circ$  is less than 190 ms. The bending strain sensitivity BS is as high as  $0.83 \text{ rad}^{-1}$ . The relative resistance  $R/R_0$  of different bending state is monitored, and the relationship between the relative resistance  $R/R_0$  and the bending angle  $\theta$  is linearly fitted. In the bending test, GE/CMC-30 film shows a stable signal for 100 cycles in forward bending  $0^\circ$  to  $90^\circ$ .

**Acknowledgements** The authors acknowledge financial support from Guangdong Fenghua Advanced Technology Holding Co., Ltd.

## Compliance with ethical standards

**Conflict of interest** The authors declare that they have no conflict of interest.

## References

1. T. Yamada, Y. Hayamizu, Y. Yamamoto et al., *Nat. Nanotechnol.* **6**, 296 (2011). <https://doi.org/10.1038/nnano.2011.36>
2. X. Wang, S. Meng, M. Tebyetekerwa et al., *Compos. A* **105**, 291 (2018). <https://doi.org/10.1016/j.compositesa.2017.11.027>
3. A.T. Sepúlveda, F. Fachin, R.G.D. Villoria et al., *Proc. Eng.* **25**, 140 (2011). <https://doi.org/10.1016/j.proeng.2011.12.035>
4. Y. Cheng, R. Wang, J. Sun, L. Gao, *Adv. Mater.* **27**, 7365 (2015). <https://doi.org/10.1002/adma.201503558>
5. C. Yan, J. Wang, W. Kang et al., *Adv. Mater.* **26**, 2022 (2014). <https://doi.org/10.1002/adma.201304742>
6. M. Amjadi, K.-U. Kyung, I. Park, M. Sitti, *Adv. Func. Mater.* **26**, 1678 (2016). <https://doi.org/10.1002/adfm.201504755>
7. H. Wu, Q. Liu, W. Du, C. Li, G. Shi, *ACS Appl. Mater. Interfaces* **10**, 3895 (2018). <https://doi.org/10.1021/acsami.7b19014>
8. Y. Zheng, Y. Li, K. Dai et al., *Compos. Sci. Technol.* **156**, 276 (2018). <https://doi.org/10.1016/j.compscitech.2018.01.019>
9. S. Gong, D.T. Lai, Y. Wang et al., *ACS Appl. Mater. Interfaces* **7**, 19700 (2015). <https://doi.org/10.1021/acsami.5b05001>
10. X. Wu, Y. Han, X. Zhang, C. Lu, *ACS Appl. Mater. Interfaces* **8**, 9936 (2016). <https://doi.org/10.1021/acsami.6b01174>
11. S.R. Forrest, *Nature* **428**, 911 (2004)
12. J.J. Park, W.J. Hyun, S.C. Mun, Y.T. Park, O.O. Park, *ACS Appl. Mater. Interfaces* **7**, 6317 (2015). <https://doi.org/10.1021/acsami.5b00695>
13. Q. Huo, J. Jin, X. Wang et al., *Mater. Res. Express* **6**, 075613 (2019). <https://doi.org/10.1088/2053-1591/ab17ac>
14. X. Li, R. Zhang, W. Yu et al., *Sci. Rep.* **2**, 870 (2012). <https://doi.org/10.1038/srep00870>
15. K.S. Kim, Y. Zhao, H. Jang et al., *Nature* **457**, 706 (2009). <https://doi.org/10.1038/nature07719>
16. O.M. Dawood, R.K. Gupta, U. Monteverde et al., *Sci. Technol. Adv. Mater.* **20**, 568 (2019). <https://doi.org/10.1080/14686996.2019.1612710>
17. Y. Pang, H. Tian, L. Tao et al., *ACS Appl. Mater. Interfaces* **8**, 26458 (2016). <https://doi.org/10.1021/acsami.6b08172>
18. Q. Wu, W. Li, Y. Wu, G. Zong, S. Liu, *Ind. Crops Prod.* **76**, 866 (2015). <https://doi.org/10.1016/j.indcrop.2015.07.047>
19. M. Yu, J. Li, L. Wang, *Chem. Eng. J.* **310**, 300 (2017). <https://doi.org/10.1016/j.cej.2016.10.121>
20. Z.-M. Huang, X.-Y. Liu, W.-G. Wu, Y.-Q. Li, H. Wang, *J. Mater. Sci.* **52**, 12540 (2017). <https://doi.org/10.1007/s10853-017-1374-1>
21. J. Chen, B. Yao, C. Li, G. Shi, *Carbon* **64**, 225 (2013). <https://doi.org/10.1016/j.carbon.2013.07.055>
22. X. Yuan, Y. Wei, S. Chen, P. Wang, L. Liu, *RSC Adv.* **6**, 64056 (2016). <https://doi.org/10.1039/c6ra12469k>
23. S. Liu, Y. Lin, Y. Wei, S. Chen, J. Zhu, L. Liu, *Compos. Sci. Technol.* **146**, 110 (2017). <https://doi.org/10.1016/j.compscitech.2017.03.044>
24. Y. Wei, S. Chen, F. Li, Y. Lin, Y. Zhang, L. Liu, *ACS Appl. Mater. Interfaces* **7**, 14182 (2015). <https://doi.org/10.1021/acsami.5b03824>
25. J.H. Lee, K.Y. Lee, M.K. Gupta et al., *Adv. Mater.* **26**, 765 (2014). <https://doi.org/10.1002/adma.201303570>
26. J. Zhao, G. Wang, R. Yang et al., *ACS Nano* (2015). <https://doi.org/10.1021/nn506341u>
27. H. Liu, Q. Li, Y. Bu et al., *Nano Energy* (2019). <https://doi.org/10.1016/j.nanoen.2019.104143>
28. T.T. Tung, R. Karunakaran, D.N.H. Tran et al., *J. Mater. Chem. C* **4**, 3422 (2016). <https://doi.org/10.1039/c6tc00607h>

**Publisher's Note** Springer Nature remains neutral with regard to jurisdictional claims in published maps and institutional affiliations.